ORIGINAL ARTICLE

ETRI Journal WILEY

Compressive sensing-based two-dimensional scattering-center extraction for incomplete RCS data

Ji-Hoon Bae[1] [iD] | Kyung-Tae Kim[2] [iD]

[1]Department of AI and Big Data Engineering, Daegu Catholic University, Gyeongsan, Rep. of Korea

[2]Electrical Engineering, Pohang University of Science and Technology, Pohang, Rep. of Korea

Correspondence
Kyung-Tae Kim, Department of Electrical Engineering, Pohang University of Science and Technology, Pohang, Rep. of Korea.
Email: kkt@postech.ac.kr

We propose a two-dimensional (2D) scattering-center-extraction (SCE) method using sparse recovery based on the compressive-sensing theory, even with data missing from the received radar cross-section (RCS) dataset. First, using the proposed method, we generate a 2D grid via adaptive discretization that has a considerably smaller size than a fully sampled fine grid. Subsequently, the coarse estimation of 2D scattering centers is performed using both the method of iteratively reweighted least square and a general peak-finding algorithm. Finally, the fine estimation of 2D scattering centers is performed using the orthogonal matching pursuit (OMP) procedure from an adaptively sampled Fourier dictionary. The measured RCS data, as well as simulation data using the point-scatterer model, are used to evaluate the 2D SCE accuracy of the proposed method. The results indicate that the proposed method can achieve higher SCE accuracy for an incomplete RCS dataset with missing data than that achieved by the conventional OMP, basis pursuit, smoothed L0, and existing discrete spectral estimation techniques.

KEYWORDS
discrete spectral estimation, iteratively reweighted least square, orthogonal matching pursuit, two-dimensional (2D) scattering-center extraction

1 | INTRODUCTION

An accurate and robust scattering-center extraction (SCE) is the main concern of target recognition and classification, as well as radar signal processing, because scattering centers (SCs) on a target can provide a rich description of the scattering mechanism of the target, even in small dimensions [1,2]. As a conventional approach for performing two-dimensional (2D) SCE, we consider the following two types of well-known discrete spectral estimation (DSE) techniques [3]: Fourier transform (FT)-based parametric techniques, such as CLEAN [4] and RELAX [5], and reliable superresolution techniques, such as multiple signal classification (MUSIC) [6] and estimation of signal parameters via rotational invariance techniques (ESPRIT) [7]. The aforementioned DSE techniques are typically subject to the condition that uniformly sampled complete radar cross-section (RCS) data are required for successful SCE. However, according to the modern inverse synthetic aperture radar (ISAR) system that employs active phased array radar techniques [8], the ISAR system in the tracking mode must switch its beam to several directions to continuously and simultaneously capture multiple targets. For each target, because of the sparse sampling, this can result in missing data in the collected RCS dataset. If data are missing, the conventional DSE techniques generally fail to extract SCs under such a nonuniform and incomplete RCS dataset [9].

Compressive-sensing (CS)-based sparse-recovery algorithms (SRAs)[10] may be good candidates for addressing this problem. This is because, compared with the well-known Nyquist sampling theory, they can reduce the amount of data required to faithfully reconstruct a signal. Because a high-frequency radar signal model, which is called the geometrical theory of diffraction (GTD) model [11], can be expressed as the summation of a few sparsely distributed SCs on a target, we can extract SCs from the undersampled incomplete dataset resulting from the missing data. SRAs can be divided into two major classes: the convex relaxation method (CRM) and the greedy pursuit method (GPM)[12]. In the case of CRM, there are two typical methods for l_1-norm optimization: basis pursuit (BP) and basis pursuit denoising [12]. However, in the case of GPM, there are different types of greedy algorithms, such as matching pursuit (MP), weak-MP, orthogonal matching pursuit (OMP), and least squares (LS) OMP [12–14]. Among the greedy algorithms, OMP is a representative algorithm that shows a relatively smaller recovery error than those of other GPM-based algorithms [12]. However, the main disadvantage of the OMP algorithm is that its accuracy in terms of radar image reconstruction is considerably sensitive to off-grid SCs and the number of SCs (nSC) [15]. Another new approach to yielding a sparse solution is the Bayesian CS, which basically adopts the relevance vector machine, in which CS has been considered from the Bayesian perspective [16]. In addition, the smoothed L0 (SL0) algorithm for CS reconstruction was proposed using a smooth measure of the l_0-norm by introducing a sequence of smoothed functions to approximate the l_0-norm [17,18]. While most research works [19–25] were performed on CS-theory-based radar image reconstruction, the capability of SCE for incomplete RCS datasets with missing data, especially for 2D SCE, has yet to be carefully and sufficiently studied.

This study aims to establish a reliable 2D SCE algorithm to enhance the SCE accuracy even when using an incomplete RCS dataset. Unlike 1D SCE [26], the adaptively sampled 2D grid suitable for sparse recovery is devised in the proposed method to substantially reduce the computational cost of 2D SCE. First, we generate an adaptively sampled grid with coarse sampling and partially fine sampling. This adaptive sampling can help significantly reduce the computational complexity of the proposed method as compared with a fully sampled fine grid. Subsequently, we implement the coarse estimation of SCs using an l_p-norm optimization technique coupled with a general peak-finding algorithm (PFA), in which the optimization technique uses the obtained 2D grid with adaptive discretization to create its own dictionary. Finally, we further improve the estimation accuracy of SCs using the OMP algorithm from an adaptively sampled Fourier dictionary. In the next section, we will describe the proposed method for 2D SCE in detail.

2 | PROPOSED METHOD

2.1 | Signal modeling

According to the point-scatterer model, the backscattered field data from L SCs at various frequencies f and look angles θ can be expressed as [27] follows:

$$e_{f^x f^y}^s = \sum_{i=1}^{L} a_i \exp\left(-j4\pi f^x/c \cdot x_i\right) \exp\left(-j4\pi f^y/c \cdot y_i\right), \quad (1)$$

where a_i denotes the amplitude of the ith SC at (x_i, y_i), $f^x = f\cos\theta$, and $f^y = f\sin\theta$. For simplicity, we consider an undamped exponential model without the angle-dependence or frequency-dependence term included in the GTD model. If the frequency bandwidth is sampled M times and the angular width sampled N times, (1) can be rewritten as follows:

$$e_{f_m^x f_n^y}^s = \sum_{i=1}^{L} a_i \exp\left(-j2\pi \frac{2f_m^x}{c} \cdot x_i\right) \exp\left(-j2\pi \frac{2f_n^y}{c} \cdot y_i\right), \quad (2)$$

where $f_m^x = f_0^x + m\Delta f^x (m = 0, 1, ..., M-1)$ and $f_n^y = f_0^y + n\Delta f^y$ $(n = 0, 1, ..., N-1)$. Without any loss of generality, we can set $f_0^x = f_0^y = 0$ to obtain the following:

$$e_{mn}^s = \sum_{i=1}^{L} a_i \exp\left(-j2\pi m \cdot \frac{x_i}{R_x}\right) \exp\left(-j2\pi n \cdot \frac{y_i}{R_y}\right), \quad (3)$$

where $R_x = c/(2\Delta f^x)$ and $R_y = c/(2\Delta f^y)$ denote the maximum unambiguous ranges in the down-range and cross-range directions, respectively. Therefore, Δf^x and Δf^y should be selected such that the maximum unambiguous ranges in both the directions include the entire target without resulting in image aliasing. If the 2D radar image domain is fully discretized using a 2D $Q \times R$ grid $(Q > M$ and $R > N)$, such as $q\Delta x(q = 0, 1, ..., Q-1)$ in the down range and $r\Delta y(r = 0, 1, ..., R-1)$ in the cross range, (3) can be rewritten as follows:

$$e_{mn}^s = \sum_{q=0}^{Q-1}\sum_{r=0}^{R-1} a_{qr} \exp\left(-j\frac{2\pi}{Q}m \cdot q\right) \exp\left(-j\frac{2\pi}{R}n \cdot r\right), \quad (4)$$
$$m = 0, 1, ..., M-1, \quad n = 0, 1, ..., N-1,$$

where Δx and Δy denote the x- and y-directional sampling grid widths for sparse recovery, respectively. Notably, the grid widths are sufficiently small to separate closely distributed SCs, namely $\Delta x < \Delta x_{Fb}$ and $\Delta y < \Delta y_{Fb}$, where Δx_{Fb} and Δy_{Fb} denote the Fb each in the down-range and cross-range domains, respectively. The resulting e_{mn}^s is merely the well-known 2D discrete FT. Therefore, (4) can be rewritten as the following matrix equation [28]:

$$[\mathbf{E}]_{M\times N} = [\mathbf{W}_x]_{M\times Q} [\mathbf{A}]_{Q\times R} [\mathbf{W}_y^T]_{R\times N}, \quad (5)$$

where $\mathbf{E} = \left(e^s_{mn}\right)$ denotes an $M \times N$ matrix representing the 2D RCS dataset, $\mathbf{A} = \left(a_{qr}\right)$ a $Q \times R$ amplitude matrix representing the 2D radar image, $\mathbf{W}_x$ an $M \times Q$ matrix representing the x-directional Fourier dictionary, and $\mathbf{W}_y$ an $N \times R$ matrix representing the y-directional Fourier dictionary. The linear equations in (5) represent an underdetermined system and have an infinite number of solutions because $Q > M$ and $R > N$. However, because the amplitudes of the SCs are sparsely distributed over a small part of the 2D radar image domain, we can solve this problem by minimizing the l_0-norm of $\mathbf{A}$ as follows:

$$(P_0): \ \min_{\underline{\sigma}} \|\underline{\sigma}\|_0 \ \text{subject to} \ \underline{e} = \mathbf{W}\underline{\sigma}, \tag{6}$$

where $\| \cdot \|_0$ denotes the l_0-norm, $\underline{e} = \text{vec}(\mathbf{E})$ an $MN \times 1$ vector representing the vectorized RCS data, $\underline{\sigma} = \text{vec}(\mathbf{A})$ a $QR \times 1$ vector representing a vectorized radar image, and $\mathbf{W} = \mathbf{W}_y \otimes \mathbf{W}_x$ an $MN \times QR$ matrix obtained by the Kronecker product of $\mathbf{W}_x$ and $\mathbf{W}_y$. In (6), vec($\bullet$) of a matrix refers to the vectorization of the matrix by stacking its columns in sequence. Using the conventional OMP algorithm, one can directly extract 2D SCs from (6) by identifying a suboptimal sparse solution using a residual. Therefore, once $\underline{\sigma}$ is solved, the 2D locations and the corresponding amplitudes can be easily obtained by mapping the 1D vectorized solutions onto the 2D parameter space.

## 2.2 | Generation of 2D adaptive grid

To separately detect the closely located SCs, the 2D parameter space (down range and cross range) should be sampled more finely, resulting in a significant increase in the size of a dictionary. To mitigate the computational complexity of the 2D optimization problem, we devise an adaptively sampled grid with a combination of coarse sampling and partially fine sampling. First, we generate a $Q_1 \times R_1$ coarse grid with sampling widths Δx_1 and Δy_1 such that $\Delta x_1 \gg \Delta x$ and $\Delta y_1 \gg \Delta y$ [see Figure 1A], namely, $Q_1 \ll Q$ and $R_1 \ll R$. The main role of the coarse grid is to guarantee the underdetermined linear system of the equation in (6) to provide unique and sparsest solution. Considering robust performance and computational complexity, we recommend that the sampling widths satisfy $0.5\Delta x_{\text{Fb}} \leq \Delta x_1 \leq \Delta x_{\text{Fb}}$ and $0.5\Delta y_{\text{Fb}} \leq \Delta y_1 \leq \Delta y_{\text{Fb}}$, both of which are, respectively, equivalent to $M \leq Q_1 \leq 2M$ and $N \leq R_1 \leq 2N$ for the size of the coarse grid. Subsequently, to obtain locally fine grids with sampling widths Δx and Δy, the following steps are presented:

● Step 1: Extract the initial locations of the SCs $\{(x'_i, y'_i)\}^{L_1}_{i=1}$ in Figure 1B by directly solving the l_0-norm optimization problem presented in (6) using the conventional OMP algorithm that uses the $Q_1 \times R_1$ coarse grid, rather than using the $Q \times R$ fine grid. Notably, an $MN \times Q_1 R_1$ coarsely sampled Fourier dictionary obtained from the 2D coarse grid can accelerate the computational speed of the OMP algorithm, resulting in performance degradation in terms of estimation accuracy.

● Step 2: Generate 2D finely sampled grids with sampling widths Δx and Δy on the basis of the extracted SCs in Step 1 [see Figure 1C]. Each fine grid, which is of rectangular
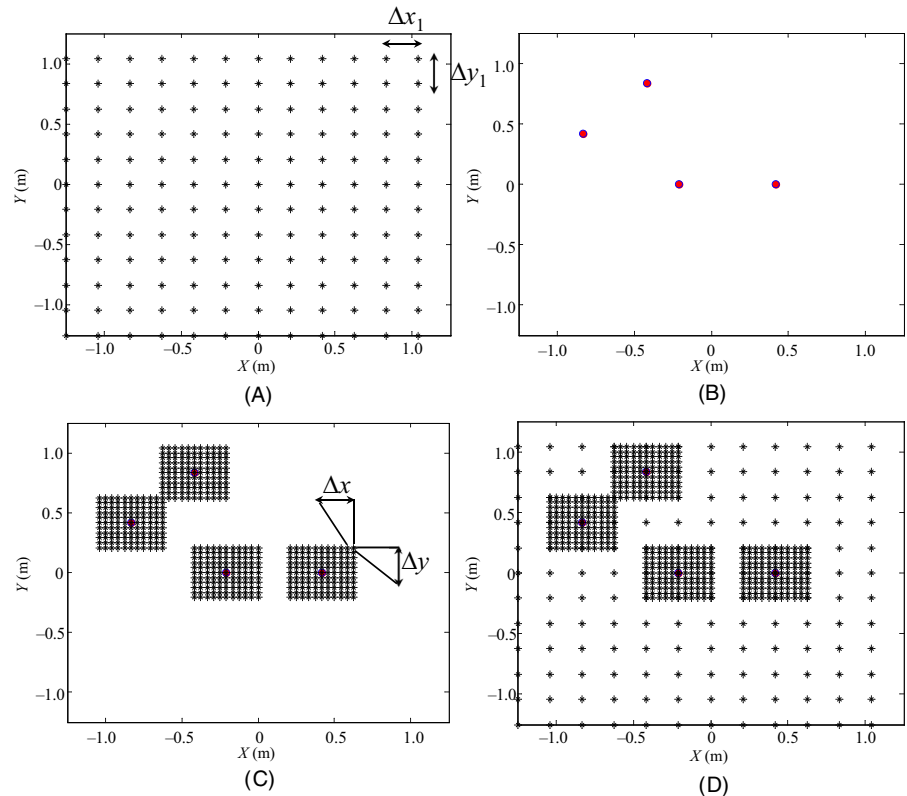
FIGURE 1 Generation of an adaptively sampled grid. (A) 2D coarse grid. (B) Initial locations of the SCs extracted using the conventional OMP algorithm. (C) Locally fine grids. (D) Adaptively sampled grid obtained from the combination of the coarse grid (see Figure 1A) and locally fine grids (see Figure 1C)
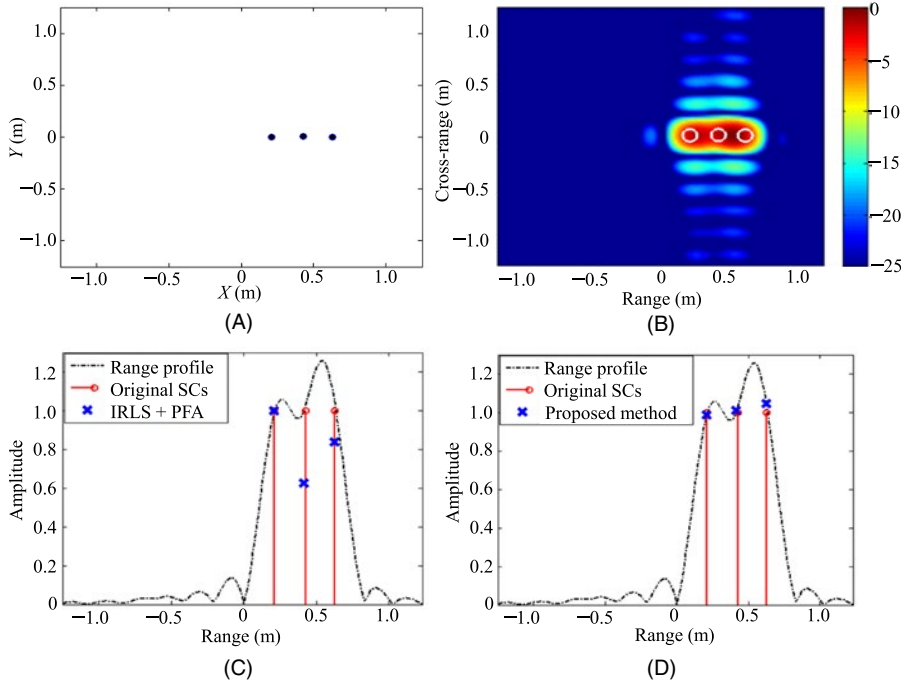
FIGURE 2 Comparative results of 2D SCE for three off-grid SCs at SNR = 20 dB (f_c = 12 GHz, BW = 720 MHz, and $\phi = -1.7189°$ to $1.4324°$). (A) Original SCs. (B) FT-based ISAR image. (C) IRLS + PFA. (D) Proposed method. Circle in white: original SCs. X marker in blue: estimated SCs

shape, is obtained using each SC, and the ranges from $(x_i' - \Delta x_{\mathrm{Fb}})$ to $(x_i' + \Delta x_{\mathrm{Fb}})$ in the down-range direction and from $(y_i' - \Delta y_{\mathrm{Fb}})$ to $(y_i' + \Delta y_{\mathrm{Fb}})$ in the cross-range direction. In the case of overlapping grid points occurring because of the overlapping of more than two grids, each resulting from the separation distance of less than Fb, the other redundant grid points should be discarded such that only one grid exists in the overlapping regions. Finally, the adaptively sampled grid that is applied to the coarse-estimation procedure (see Section 2.3) in the proposed method is created by combining the coarse grid with the locally fine grids (see Steps 1 and 2), as depicted in Figure 1D.

2.3 | Coarse estimation of 2D SCs

From (6), the coarse-estimation procedure for a 2D SCE using the proposed method can be stated as follows:

• Step 1: Generate an initial dictionary using the 2D grid with adaptive sampling obtained in Section 2.2. Notably, each grid point on the 2D grid produces a single $MN \times 1$ $\mathbf{W}_A$ basis function belonging to $\mathbf{W}_A$.
• Step 2: Calculate $\underline{\sigma}$ using the dictionary $\mathbf{W}_A$ in Step 1 by solving the l_p-norm optimization problem (P_p) as follows:

$$(P_p): \min_{\underline{\sigma}} \|\underline{\sigma}\|_p^p \text{ subject to } \|\underline{e} - \mathbf{W}_A \underline{\sigma}\|_2^2 \le \varepsilon_0, \quad (7)$$

where $\underline{\sigma}$ denotes the vectorization of the amplitudes at all the sampled 2D spatial positions of the adaptive grid; in

addition, $0 < p \le 1$, and ε_0 denotes the error tolerance with a low positive value. To solve the problem P_p in this study, we adopt the method of iteratively reweighted least square (IRLS) that minimizes the weighted LS via iterative re-weighting [10,29].

• Step 3: Normalize the obtained from Step 2 as $\underline{\sigma}' = \underline{\sigma} / \max |\underline{\sigma}|$, and apply a thresholding operator using a threshold level α_{th} to the normalized $\underline{\sigma}$ as follows:

$$\underline{\sigma}'_{\mathrm{th}} = \begin{cases} \underline{\sigma}'_{\mathrm{th}} = \underline{\sigma}', \text{ if } \underline{\sigma}' \ge \alpha_{\mathrm{th}} \\ \underline{\sigma}'_{\mathrm{th}} = 0, \text{ otherwise.} \end{cases} \quad (8)$$

• Step 4: Extract the vectorized locations of the SCs from $\underline{\sigma}'_{\mathrm{th}}$ by using a general 1D peak-finding algorithm (PFA). Subsequently, the 2D locations $\{(x_i'', y_i'')\}_{i=1}^{L_2}$ can be simply obtained from the vectorized locations.
• Step 5: Generate the following $MN \times L_2$ dictionary ($\mathbf{W}_N$) by using the extracted $\{(x_i'', y_i'')\}_{i=1}^{L_2}$ from Step 4 as follows:

$$\mathbf{W}_N = [\underline{f}(x_1'', y_1'') \underline{f}(x_2'', y_2'') \cdots \underline{f}(x_{L_2}'', y_{L_2}'')], \quad (9)$$

where the basis function $\underline{f}(x_i'', y_i'')$ is defined as follows:

$$\underline{f}(x_i'', y_i'') = [\underline{w}_i(0, 0), \underline{w}_i(1, 0), ..., \underline{w}_i(M-1, 0),$$
$$\underline{w}_i(0, 1), \underline{w}_i(1, 1), ..., \underline{w}_i(M-1, 1), ...,$$
$$\underline{w}_i(0, N-1), \underline{w}_i(1, N-1), ..., \underline{w}_i(M-1, N-1)]^T,$$
$$i = 1, 2, ..., L_2, \quad (10)$$

where $\underline{w}_i(m,n) = \exp[-j2\pi(m\cdot x_i''/R_x + n\cdot y_i''/R_y)]$, $m = 0, 1, \ldots, M - 1, n = 1, 2, \ldots, N - 1$.

Generally, the direct extraction of SCs by using PFA cannot guarantee reliable SCE, although the amplitudes of the SCs can also be extracted using Step 4. It is because PFA easily suffers from noisy environments because of the undesired local peaks due to side lobes or noises, although α_{th} is considered as well. For example, Figure 2 depicts the extracted three SCs (X marker in blue) obtained via direct SCE by using IRLS coupled with only PFA from Steps 1 to 4, and those using the proposed method when three SCs are arranged alongside one another (see Figure 2A). Here, the range profile (shown as the dashed line in black) is obtained by cutting the conventional FT-based ISAR image (see Figure 2B) along the down-range direction. Clearly, the estimation accuracy of the amplitudes (see Figure 2C) is inferior to that obtained using the proposed method (see Figure 2D) irrespective of the correct estimation of the locations (see Figure 2C). To achieve further improvement in the SCE accuracy, we must perform an additional procedure for the fine estimation of the amplitudes when extracting the desired locations from the redundant locations of the SCs in Step 4 simultaneously. Therefore, we generate an adaptively sampled Fourier dictionary $\mathbf{W}_N$ indicated in Step 5 as the medium to establish a link between the coarse-estimation procedure and next fine-estimation step in Section 2.4.

2.4 | Fine estimation of 2D SCs

The fine-estimation procedure using $\mathbf{W}_N$ to improve the SCE accuracy can be described as follows:

- Step 1: Assume $k = 1$. Estimate the location $(\hat{x}_1'', \hat{y}_1'')$ using (11), where the initial residual $\underline{r}^0 = \underline{e}$. One has the following:

$$(\hat{x}_k'', \hat{y}_k'') = \max_{(x_i'', y_i'')} \left| \underline{f}(x_i'', y_i'')^H \cdot \underline{r}^{k-1} \right|, \quad i = 1, 2, \ldots, L_2, \quad (11)$$

where $\{\underline{f}(x_i'', y_i'')\}_{i=1}^{L_2}$ belong to $\mathbf{W}_N$. Notably, the extracted basis function $[\underline{f}(\hat{x}_1'', \hat{y}_1'')]$ corresponding to $(\hat{x}_1'', \hat{y}_1'')$ is not involved in Step 4 of the estimation process.

- Step 2: Estimate the amplitudes $\underline{\sigma}^1$ by solving the following optimization problem, where the initial $\mathbf{\Psi}^0$ denotes an empty matrix: $P_2[\hat{\sigma}_1'', \hat{\sigma}_2'', \ldots, \hat{\sigma}_k'']^T$

$$(P_2): \quad \min_{\underline{a}^k} \left\| \underline{e} - \mathbf{\Psi}^k \underline{\sigma}^k \right\|_2^2, \quad (12)$$

where $\mathbf{\Psi}^k = [\mathbf{\Psi}^{k-1} \underline{f}(\hat{x}_k'', \hat{y}_k'')]$ and $\underline{\sigma}^k = \begin{bmatrix} \sigma^{k-1} \\ \hat{\sigma}_k'' \end{bmatrix} = [\hat{\sigma}_1'', \hat{\sigma}_2'', \ldots, \hat{\sigma}_k'']^T$. The aforementioned optimization problem can then be solved using the least-square (LS) estimation in (13) as follows:

$$\underline{\sigma}^k = \left((\mathbf{\Psi}^k)^H \mathbf{\Psi}^k \right)^{-1} (\mathbf{\Psi}^k)^H \underline{e}. \quad (13)$$

- Step 3: Compute the residual $\underline{r}^1$ from (14) by using $\hat{x}_1'', \hat{y}_1''$ and $\hat{\sigma}_1''$ obtained from Steps 1 and 2.

$$\underline{r}^k = \underline{e} - \sum_{i=1}^{k} \hat{\sigma}_1'' \exp\left[-j2\pi(m\cdot \hat{x}_i''/R_x + n\cdot \hat{y}_k''/R_y)\right]. \quad (14)$$

- Step 4: Assume $k = 2$. Estimate location $(\hat{x}_2'', \hat{y}_2'')$ using (11) by using the residual $\underline{r}^1$ obtained from Step 3. Obviously, the extracted basis function $[\underline{f}(\hat{x}_2'', \hat{y}_2'')]$ at this stage is not involved in the next estimation process in (11).
- Step 5: Calculate $\underline{\sigma}^2$ from (13) by using the basis functions $\{\underline{f}(\hat{x}_i'', \hat{y}_i'')\}_{i=1}^{2}$ corresponding to $\{(\hat{x}_i'', \hat{y}_i'')\}_{i=1}^{2}$ obtained from Steps 1 and 4. Notably, the previously estimated amplitude $\underline{\sigma}^1$ in Step 2 is reestimated in this step such that the column space of $\mathbf{\Psi}^2$ should be orthogonal to residual $\underline{r}^1$. Therefore, the reestimation process for obtaining $\underline{\sigma}^k$ at each iteration enables us to accomplish further improvement in determining the accuracy of the amplitudes of the SCs as compared with the direct estimation of SCs by using the PFA, as depicted in Figure 2.
- Step 6: Compute residual $\underline{r}^2$ from (14) by using $\{(\hat{x}_i'', \hat{y}_i'')\}_{i=1}^{2}$ and $\underline{\sigma}^2$ obtained from Steps 1, 4, and 5.
- Step 7: Repeat Steps 1–7 until the following cost function C between the $(k-1)$th and kth iterations is below some predefined small quantity δ. Namely, unlike most GPM-based conventional greedy algorithms, which generally adopt the stopping rule (C_g) using only the residual (ie, $C_g = \| \underline{r}^k \|_2 < \delta$), we decide when to terminate the iterations by checking the following relative change in the cost function:

$$C = \left| \left\| \underline{r}^k \right\|_2 - \left\| \underline{r}^{k-1} \right\|_2 \right| < \delta. \quad (15)$$

This stopping rule in C allows us to determine the threshold more easily than C_g for practical convergence. Regarding the stopping criterion using the relative change, the selection of $0.001 \leq \delta \leq 0.01$ is recommended to terminate the iterations in the fine estimation of the proposed method. Obviously, the recommended threshold can be slightly adjusted depending on the desired accuracy of the optimal solution. Therefore, if the procedure is implemented using L_3 iterations satisfying (15), $\{(\hat{x}_i'', \hat{y}_i'')\}_{i=1}^{L_3}$ and $\{\hat{\sigma}_i''\}_{i=1}^{L_3}$ are the estimated locations and
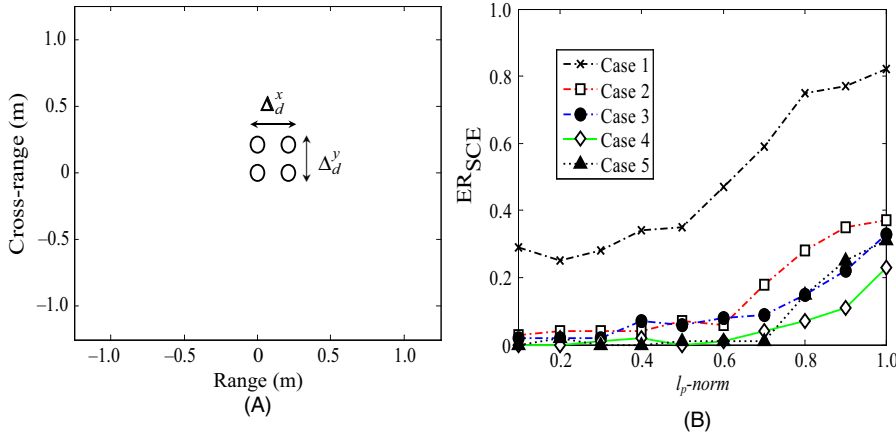
FIGURE 3 ER_{SCE} with respect to the p values. (A) Four closely located SCs. (B) ER_{SCE} versus p at SNR = 20 dB (= 12 GHz, BW = 720 MHz, $\phi = -1.7189°$ to $1.4324°$, $\Delta x_{Fb} = \Delta y_{Fb} = 0.2083$ m, and $M = N = 12$). Case 1: $\Delta_d^x = 0.6\Delta x_{Fb}$ and $\Delta_d^y = 0.6\Delta y_{Fb}$, Case 2: $\Delta_d^x = 0.7\Delta x_{Fb}$ and $\Delta_d^y = 0.7\Delta y_{Fb}$, Case 3: $\Delta_d^x = 0.8\Delta x_{Fb}$ and $\Delta_d^y = 0.8\Delta y_{Fb}$, Case 4: $\Delta_d^x = 0.9\Delta x_{Fb}$ and $\Delta_d^y = 0.9\Delta y_{Fb}$, Case 5: $\Delta_d^x = 1.0\Delta x_{Fb}$ and $\Delta_d^y = 1.0\Delta y_{Fb}$

amplitudes of the SCs, respectively. Owing to the fine-estimation procedure presented in Steps 1–7, the advantages of the proposed method can be summarized as follows: First, nSC can be automatically determined using the residual and the stopping criterion presented in (15) because the desired basis functions, as well as the locations of the SCs, can be efficiently extracted from the redundant $\mathbf{W}_N$ via an iterative search by the largest projection, where the inner product between a residual and the basis function is maximized. Second, the estimation accuracy of the amplitudes of the SCs can be further improved by using the reestimation process with the LS estimation presented in (13). Finally, the size of the adaptively sampled Fourier dictionary, that is, $MN \times L_2$, is substantially smaller than that of the original Fourier dictionary, $MN \times QR$, as $L_2 \ll QR$ in general. This can result in a significantly reduced search space of the locations in (11) for the fine-estimation process. Therefore, using the additional fine-estimation procedure in the proposed method, an accurate estimation of the scattering properties, namely, locations and amplitudes can be achieved as compared with that achieved using only PFA from the reconstructed ISAR image; however, it results in a slight increase in the computational complexity.

2.5 | Determination of l_p-norm for the proposed method

To implement 2D SCE in the proposed method, it is first necessary to determine the design parameter p-norm, as defined in (7). For example, Figure 3 depicts the SCE error rate ER_{SCE} for a variation in the l_p-norm when four closely located SCs of equal amplitude are considered for several distances (Δ_d^x and Δ_d^y). ER_{SCE} is defined as follows:

$$ER_{SCE} = \begin{cases} 0, & \text{if } \left[(\hat{x}_i'', \hat{y}_i'') - (x_i, y_i)\right] \leq (\pm\Delta r_x, \ \pm\Delta r_y) \\ 1, & \text{otherwise}, i = 1, 2, ..., L, \end{cases} \quad (16)$$

where Δr_x and Δr_y denote the threshold distances for distinguishing the inaccurately estimated 2D SCs. Specifically, $ER_{SCE}= 0$ means that all the extracted SCs ($\{(\hat{x}_i'', \hat{y}_i'')\}_{i=1}^L$) are successfully identified within the thresholds $[\leq (\pm\Delta r_x, \pm\Delta r_y)]$; otherwise, $ER_{SCE}= 1$. This implies that if at least one more SC is incorrectly detected beyond the thresholds $[> (\pm\Delta r_x, \pm\Delta r_y)]$, ER_{SCE} is set to 1. In this experiment, to determine the separability of the extracted 2D SCs, the thresholds $\pm\Delta r_x$ and $\pm\Delta r_y$ are set to $\pm 0.5\Delta_d^x$ and $\pm 0.5\Delta_d^y$, respectively, for each case. As depicted in Figure 3B, the SCE accuracies for all the cases deteriorate gradually for the increased P values. Specifically, when P increases from 0.6 to 1.0, severe performance degradation can be observed as Δ_d decreases. Contrarily, no noticeable deterioration in accuracy is observed for most cases when p increases to a value below approximately 0.6, although the accuracy fluctuates slightly. Notably, the l_1-norm minimization can be inadequate for extracting the closely located SCs in terms of separability. Therefore, the selection of $p \leq 0.6$ is adequate for performing efficient 2D SCE using the proposed method. In this study, with a view to achieving robust SCE accuracy, we used $p = 0.3$ for all the experimental results.

3 | RESULTS

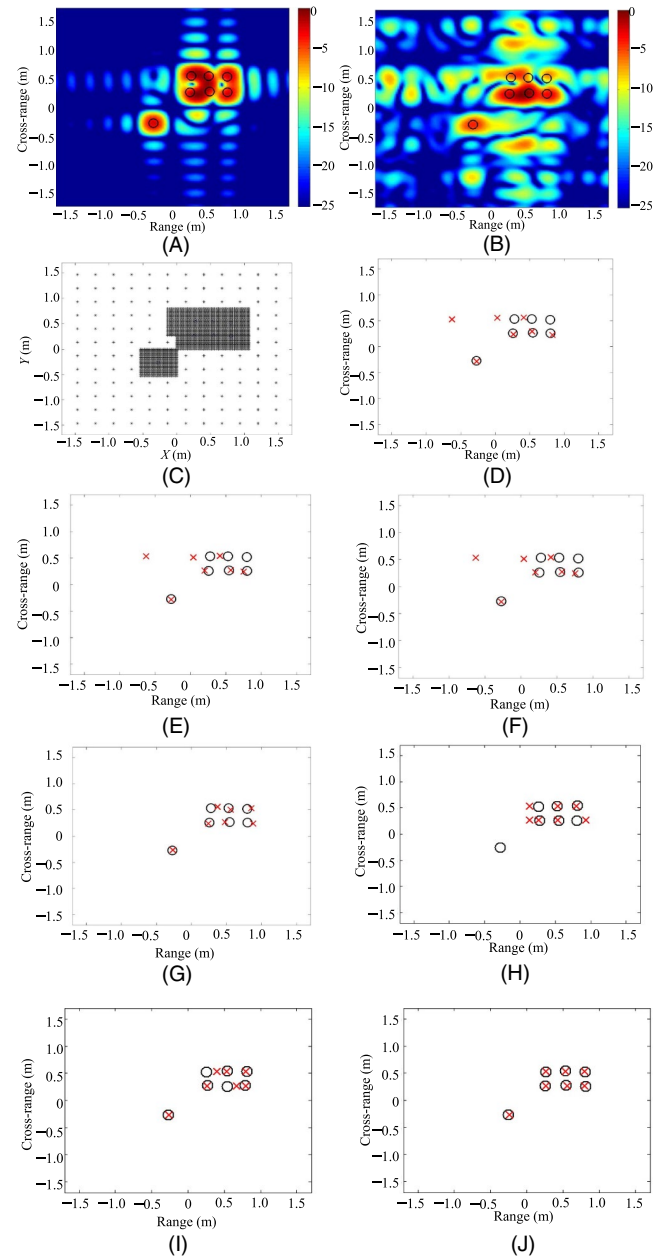### 3.1 | 2D SCE using incomplete RCS dataset

To examine the 2D SCE capability of the proposed method in terms of missing data, we used an incomplete RCS dataset by eliminating randomly selected data. Namely, we randomly selected row and column positions in the 2D complete RCS dataset; subsequently, we eliminated all the RCS data belonging to the selected row and column positions. Therefore, we calculated the number of missing data points as $p_m = (M \times N - (M - M') \times (N - N')) / (M \times N)$, where M and N denote the number of rows and columns in the complete 2D RCS dataset, respectively, and M' and N' the

number of deleted rows and columns, respectively. Notably, the generation of the adaptively sampled grid and the coarse- and fine-estimation procedures described in Sections 2.2, 2.3, and 2.4 are directly applicable to the incomplete RCS data case by using the $(M - M') (N - N') \times 1$ vectorized $\underline{\sigma}$, as well as the two redundant dictionaries $\mathbf{W}_A$ and $\mathbf{W}_N$ with $(M - M') (N - N') \times 1$ basis functions, as is the case for the complete RCS data.

First, we assume that seven off-grid SCs of equal amplitude are distributed in a 2D image domain (circle in Figure 4A), where the x- and y-grid width are equal to Δx_{Fb} and Δy_{Fb}, respectively. Because of the closely located six SCs, the conventional FT-based ISAR image cannot separate all the SCs. Figure 4B depicts an ISAR image when using the incomplete RCS data with $p_m = 55.5\%$. Notably, the resultant ISAR image is generally corrupted, and a large number of side lobes with high levels are observed in the image domain as well. Therefore, to resolve all the SCs, an adaptively sampled grid in Figure 4C is generated and used for the proposed method.

Considering the tradeoff between the SCE accuracy and computational complexity, we used the $M \times N$ coarse grid with $\Delta x_1 = \Delta x_{Fb}$ and $\Delta y_1 = \Delta y_{Fb}$, along with the locally fine grids with $\Delta x = \Delta x_{Fb}/10$ and $\Delta y = \Delta y_{Fb}/10$, for the adaptively sampled grid. For OMP, BP, and SL0, a fully sampled fine grid was generated by discretizing the image domain with $\Delta x = \Delta x_{Fb}/10$ and $\Delta y = \Delta y_{Fb}/10$. The PFA described in Section 2.3 was applied to the estimation of SCs for both BP and SL0. The SCs extracted using each method for the incomplete RCS data are depicted in Figures 4D–4J. For the three DSE methods, namely, CLEAN, RELAX, and ESPRIT, the conventional linear interpolation (LIP) method was applied to the missing data in advance so as to provide a uniform dataset before using the incomplete RCS dataset for 2D SCE. Particularly, for the two FT-based DSE methods, namely, CLEAN and RELAX, we also applied zero padding 100 times to the uniform dataset. This is typically done because of the need for sufficient zero padding to obtain an accurate estimate of closely located SCs in their own SCE procedures. Nevertheless, from Figure 4, it is evident that the three DSE methods cannot accurately resolve all SCs as compared with OMP, BP, SL0, and the proposed method. Compared with OMP and the proposed method, the locations of some SCs for BP and SL0 were not properly estimated because of the limitation of the PFA, as described in Figure 2. Although OMP is capable of extracting most SCs close to the original SCs (see Figure 4G), its accuracy is inferior to that of the proposed method (see Figure 4J). In addition, when ER_{amp} is defined as in (17), the comparative amplitude accuracy results obtained for each SRA are represented in Table 1. One has the following:

$$ER_{amp} = \frac{1}{N} \sum_{n=1}^{N} \left(|a_n^r| - |a_n^{est}| \right)^2, \quad (17)$$

FIGURE 4 Comparative results of 2D SCE for seven off-grid SCs ($f_c = 12$ GHz, BW = 562.5 MHz, $\phi = -1.3429°$ to 1.1638°, $\Delta x_{Fb} = \Delta y_{Fb} = 0.2667$ m, and $M = N = 15$). (A) Original FT-based ISAR image using the complete RCS data. (B) FT-based ISAR image using the incomplete RCS data with $p_m = 55.5\%$. (C) Adaptively sampled grid. (D) CLEAN + LIP. (E) RELAX + LIP. (F) ESPRIT + LIP. (G) OMP. (H) BP. (I) SL0. (J) Proposed method. Circle in black: original SCs. X marker in red: estimated SCs [Colour figure can be viewed at wileyonlinelibrary.com]

where a_n^r and a_n^{est} denote the real and estimated amplitudes of the nth SC, respectively. In this experiment, instead of using PFA, we applied the same fine estimation using the OMP procedure in Section 2.4 for both BP and SL0 to overcome the drawback of PFA. Although BP and SL0 use the fine-estimation procedure for SCE, the proposed method clearly surpassed both the methods,

as well as the OMP procedure, owing to the proposed coarse- and fine-estimation procedures using the adaptively sampled grid, as shown in Table 1. The average computation time for each method for 2D SCE using the incomplete dataset is listed in Table 2.

Subsequently, to quantitatively evaluate the SCE accuracy of each method from the incomplete RCS dataset, we define the following performance measure in the 2D image domain:

$$\text{MSE}_{2D} = \frac{1}{MN} \sum_{m=1}^{M} \sum_{n=1}^{N} (|I(m,n)| - |I^r(m,n)|)^2, \quad (18)$$

where $|I(m,n)|$ denotes the magnitude of an ISAR image with original SCs and $|I^r(m,n)|$ the magnitude of an ISAR image regenerated from the estimated SCs. Moreover, I^r is obtained from the regenerated 2D RCS dataset by substituting the estimated SCs in (2). A total of 25 SCs with random amplitudes ranging from 0.5 to 1 are assumed to be randomly distributed in the 2D image domain, where the x-grid width $= \Delta x_{\text{Fb}}$ and the y-grid width $= \Delta y_{\text{Fb}}$, as depicted in Figure 4. Subsequently, all the on-grid SCs are perturbed by $(\pm \varepsilon_x, \pm \varepsilon_y)$ $= (\pm 5\%, \pm 5\%)$. The reconstruction accuracies of all the methods are compared with one another with respect to p_m are compared in Figure 5. In this experiment, the average result for 100 independent realizations per p_m was presented when nSC = 25 was used for the 2D SCE of each method. In addition, two types of interpolations—nearest-neighbor interpolation and spline interpolation—were additionally considered for 2D SCE in RELAX. The fine-estimation procedure in Section 2.4 was also applied to both BP and SL0 for 2D SCE. As p_m increased, the performance of the FT-based RELAX was significantly degraded, as expected. This phenomenon proves that the FT-based operation cannot deal with nonuniformly sampled datasets caused by missing data, although the missing data are interpolated in advance using conventional interpolation methods. However, the proposed method is very robust to incomplete RCS datasets, and the accuracy of the proposed method is also better than that of OMP, BP, and SL0.

TABLE 1 ER$_{\text{amp}}$ values from the average results of 100 independent realizations for 7 SCs when $p_m = 55.5\%$

| Item	OMP	BP	SL0	Proposed method
Amplitude accuracy	0.29	0.385	0.214	0.0014

3.2 | Measured results

To further validate the proposed method in a realistic environment, the measured RCS data of a scaled aircraft model (see Figure 6B) at the POSTECH compact range facility (see Figure 6A) [30] were used for 2D SCE. The RCS data of the target were measured over a frequency band of 8.3 GH–12.3 GHz and $\pm 4.8°$ aspect region with respect to the head of the target. The measurement polarization was vertical. The original FT-based ISAR image using the measured complete RCS data and nine SCs extracted using the proposed method (nSC = 9) under the aforementioned experimental conditions are depicted in Figures 6C and 6D, respectively. Notably, the geometry of the target, including the cockpit and two tails, is well indicated in the 2D image domain. As depicted in Figure 6D, the predicted nSC was automatically determined by the stopping criterion C in (15) ($\delta = 0.005$), and the 2D adaptive grid composed of the M x N coarse grid ($\Delta x_1 = \Delta x_{\text{Fb}}$ and $\Delta y_1 = \Delta y_{\text{Fb}}$) and locally fine grids ($\Delta x = \Delta x_{\text{Fb}}/5$ and $\Delta y = \Delta y_{\text{Fb}}/5$) was used to build the adaptively sampled Fourier dictionary in the proposed method. Figure 6E depicts an incomplete RCS dataset with $p_m = 43.8\%$ by excluding the randomly selected data from the measured complete RCS dataset. Upon applying the proposed method to the measured incomplete RCS dataset, the extracted SCs depicted in Figure 6F (X marker in
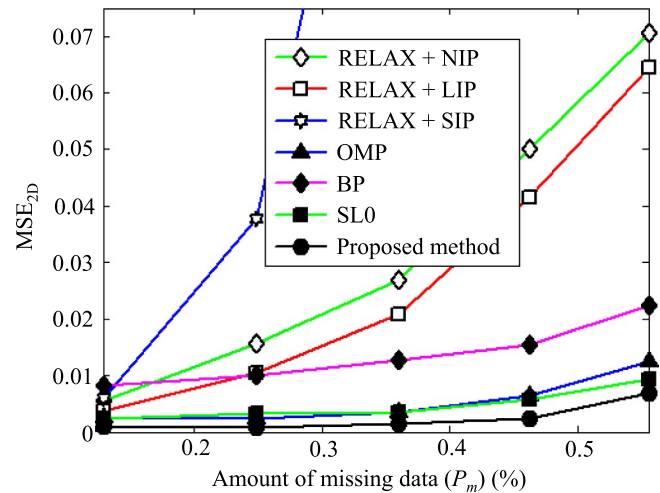

FIGURE 5 MSE$_{2D}$ vs p_m when nSC = 25 ($p_m = 12.8\%$ with $M' = N' = 1$, $p_m = 24.8\%$ with $M' = N' = 2$, $p_m = 36\%$ with $M' = N' = 3$, $p_m = 46.2\%$ with $M' = N' = 4$, and $p_m = 55.5\%$ with $M' = N' = 5$)

TABLE 2 Average computation times (s) ($N = 10$) for each method using a PC with an Intel i7-4930K CPU and 64 GB RAM running MATLAB R2014a

Item	CLEAN +LIP	RELAX +LIP	ESPRIT +LIP	OMP	BP	SL0	Proposed method
Average time (s)	0.557	24.27	0.031	0.087	17.06	2.55	0.908

FIGURE 6 2D SCE using the proposed method for the measured RCS data. (A) POSTECH compact range [30]. (B) Geometry of the scaled aircraft model, F-117 (79 cm × 118 cm). (C) Original FT-based ISAR image. (D) SCs extracted using the complete RCS data. (E) Incomplete RCS dataset with $p_m = 43.8\%$ ($M = N = 60$ and $M' = N' = 15$). (F) SCs extracted using the incomplete RCS dataset in Figure 6E
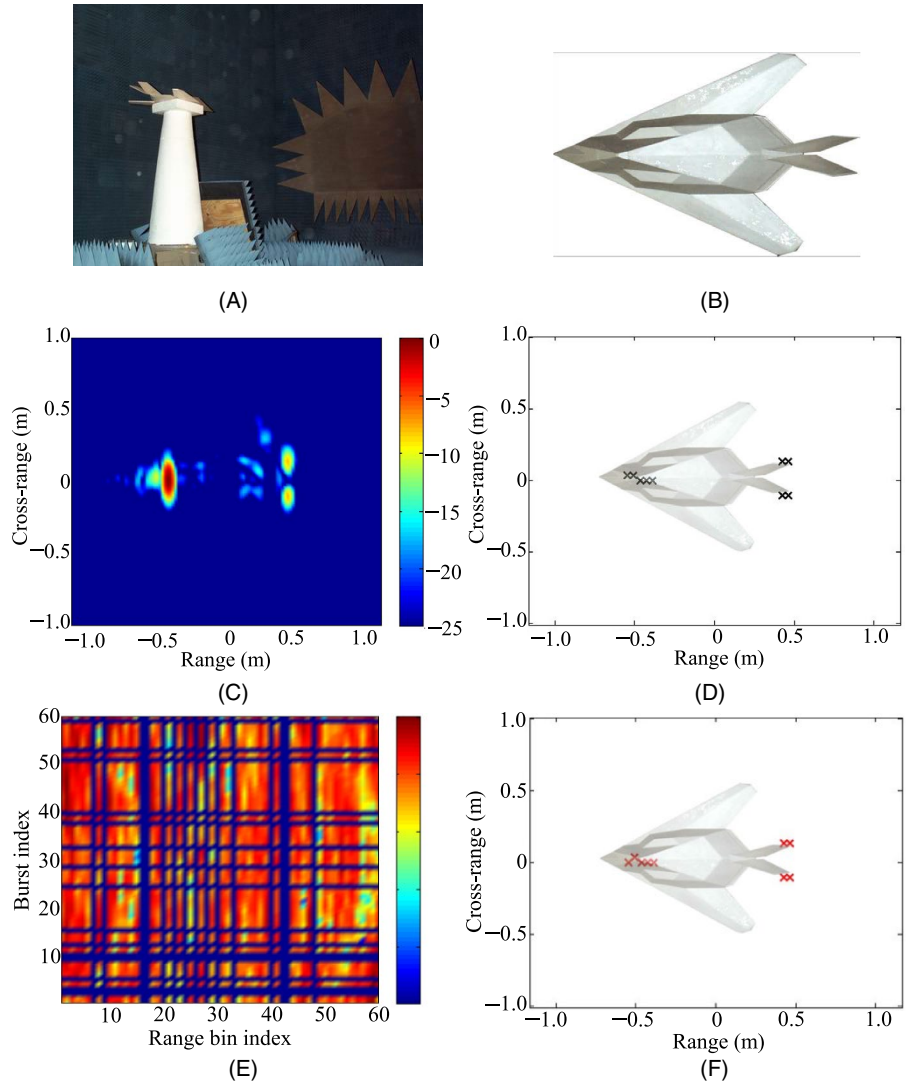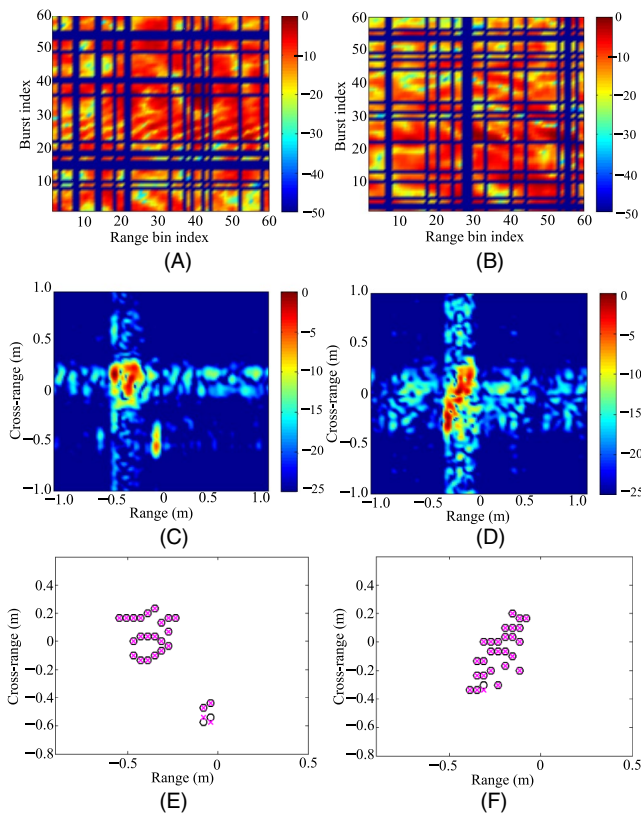

FIGURE 7 2D SCE using the proposed method for the measured RCS data. (A) Geometry of the scaled aircraft model, F-14 (146 × 131 cm). (B) Geometry of the scaled aircraft model, MIG-29 (79 × 118.5 cm). (C) Original FT-based ISAR image and its extracted SCs with nSC = 25 for the target (see Figure 7A). (D) Original FT-based ISAR image and its extracted SCs with nSC = 27 for the target (see Figure 7B). Circle in black: SCs estimated using the complete dataset
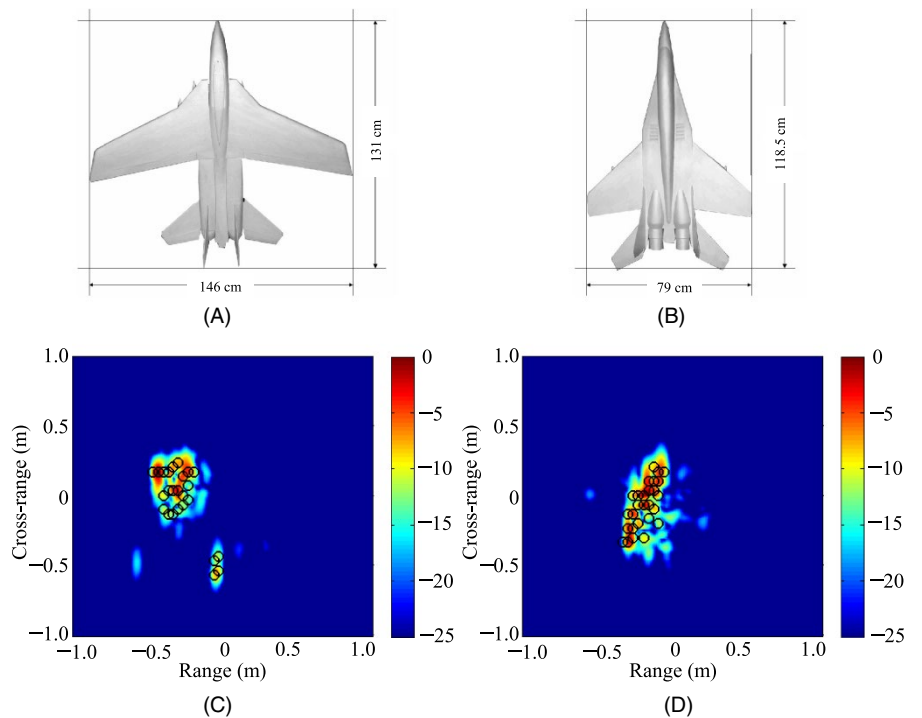
red) were obtained, showing reliable SCE accuracy performance as compared with that of the results presented in Figure 6D.
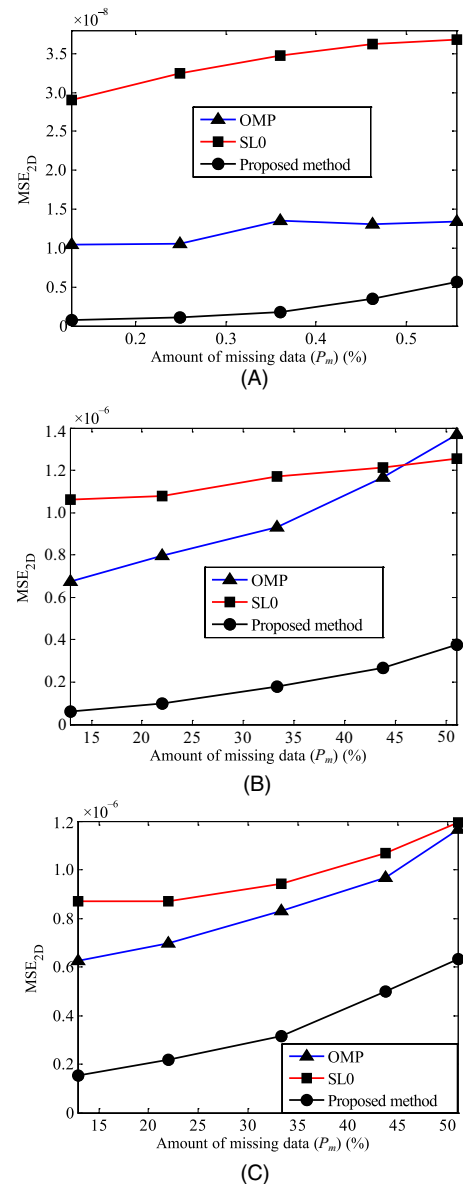
Because the target in Figure 6B has the geometry of a stealth aircraft, we considered another two targets with more SCs to verify the capability of 2D SCE using the proposed method, as depicted in Figures 7A and 7B. On the basis of the same experimental conditions as those in Figure 6, the original FT-based ISAR images using the measured complete RCS dataset are depicted in Figure 7C with the estimated nSC = 25 and Figure 7D with the estimated nSC = 27 (circle in black) using the same stopping criterion C ($\delta = 0.005$). In this experiment, the azimuth aspect varied from 30.2° to 59.8° with respect to the head of the target. The measurement polarization was horizontal for the target in Figure 7A and vertical for that in Figure 7B. The same 2D adaptive grid composed of the $M \times N$ coarse grid ($\Delta x_1 = \Delta x_{Fb}$ and $\Delta y_1 = \Delta y_{Fb}$) and locally fine grids ($\Delta x = \Delta x_{Fb}/5$ and $\Delta y = \Delta y_{Fb}/5$) was

used to build the adaptively sampled Fourier dictionary in the proposed method. Because of the adaptive grid generation, the computation time of the proposed method using the adaptively sampled grid ($T_c = 146.5$ s for Figure 7A and $T_c = 152.4$ s for Figure 7B) was considerably reduced as compared with the time taken upon using the fully sampled fine grid ($T_c = 8,401.5$ s for Figure 7A and $T_c = 8,450.8$ s for Figure 7B).

Upon applying the proposed method to the two measured incomplete RCS datasets with the same $p_m = 43.8\%$ (see Figures 8A and 8B), the extracted SCs [X marker in red in Figures 8E and 8F] are obtained and overlapped with the corresponding SCs estimated using the complete RCS

FIGURE 8 2D SCE using the proposed method for the measured incomplete RCS data. (A) Incomplete RCS dataset with $p_m = 43.8\%$ for the target ($M = N = 60$ and $M' = N' = 15$, see Figure 7A). (B) Incomplete RCS dataset with $p_m = 43.8\%$ for the target (see Figure 7B). (C) ISAR image using the incomplete RCS dataset (see Figure 7A). (D) ISAR image using the incomplete RCS dataset (see Figure 7B). (E) Extracted SCs using the incomplete RCS data (see Figure 7A). (F) SCs extracted using the incomplete RCS data (see Figure 7B). Circle in black: SCs estimated using the complete dataset. X marker in red: estimated SCs using the incomplete dataset

FIGURE 9 MSE_{2D} vs p_m ($P_m = 12.9\%$ with $M' = N' = 4$, $P_m = 22\%$ with $M' = N' = 7$, $p_m = 33.3\%$ with $M' = N' = 11$, $p_m = 43.8\%$ with $M' = N' = 15$, and $p_m = 51\%$ with $M' = N' = 18$). (A) Target in Figure 6B. (B) Target in Figure 7A. (C) Target in Figure 7B

data [circle in black in Figures 8E and 8F). Consequently, the extracted SCs for the three targets (see Figure 6F and X marker in Figures 8E and 8F) are consistent with the originally estimated SCs (see Figure 6D and circle in Figures 8E and 8F, respectively), although the incomplete datasets that produce distorted ISAR images, such as those in Figures 8C and 8D, are used for 2D SCE in the proposed method.

To evaluate the performance of the proposed method for the measured data, we first constructed different incomplete RCS datasets ranging from 12.9% to 51%. Subsequently, we calculated the MSE_{2D} values from the average result of 100 independent realizations for each p_m value (see Figure 9). In this experiment, we did not consider conventional DSE methods to obtain the comparative result because the conventional DSE methods are generally expected to fail in extracting SCs with incomplete RCS datasets (see Figures 4 and 5). Regarding the nSCs, note that OMP, SL0 with the fine-estimation procedure, and the proposed method depicted in Figure 9 use the same stopping criterion presented in (15) ($\delta = 0.005$) at every realization per p_m, as there is no prior knowledge of the true nSC of the target in real situations. Consequently, as depicted in Figure 9, the proposed method exhibits good performance in terms of SCE accuracy over the measured incomplete RCS dataset of a realistic target.

4 | Conclusion

A robust 2D SCE method based on the CS theory was proposed for incomplete RCS datasets. The proposed method comprised three parts: 1) generation of the adaptively sampled grid with a combination of coarse sampling and partially fine sampling in the 2D image domain; 2) coarse estimation of SCs using the l_p-norm optimization technique (IRLS) coupled with PFA from the 2D adaptive grid; and 3) fine estimation of SCs with the help of the OMP algorithm using the adaptively sampled Fourier dictionary. Because of the adaptive grid generation, the computational complexity of the proposed method was significantly reduced as compared with that using the fully sampled fine grid. Furthermore, because of the fine-estimation procedure, using the proposed method, we could achieve a more accurate estimate of SCs as compared with that achieved via the SCE method using only PFA. Another advantage is that the proposed method can automatically estimate nSC by implementing the stopping criterion using the relative change. To quantitatively validate the 2D SCE capability of the proposed method, we adopted ER_{SCE} and MSE_{2D} as the performance measures and compared the accuracy of the proposed method with those of the existing 2D SCE methods. The results showed that the proposed method generally achieves high SCE accuracy for incomplete RCS datasets with missing data, as compared with those of the other methods considered in this study.

Finally, the proposed method for 2D SCE adopted the simplified GTD model without frequency-dependence and angle-dependence terms. Notably, the original GTD model is a more accurate model to express the backscattered field of a target, although the proposed method using the simplified model showed reasonable results for 2D SCE. However, the above-mentioned two dependence terms make it challenging to directly apply the CS theory to 2D SCE, in general, in terms of reliable sparse recovery and efficient computational complexity. In the future, we will consider the extension to 2D SCE using the GTD model to combine it with the proposed CS-theory based method.

ORCID
Ji-Hoon Bae https://orcid.org/0000-0002-0035-5261
Kyung-Tae Kim https://orcid.org/0000-0003-1200-5282

REFERENCES
1. B. Ulug and S. C. Ahalt, *Efficient ATR using compression*, IEEE Trans. Aerosp. Electron. Syst. **33** (1997), no. 4, 1199–1211.
2. K.-T. Kim, D.-K. Seo, and H.-T. Kim, *Radar target identification using one-dimensional scattering centers*, IEE Proc. Radar Sonar Navig. **148** (2001), no. 5, 285–296.
3. S. M. Kay, Modern spectral estimation: Theory and application, Prentice-Hall, Upper Saddle River, NJ, 1999.
4. J. Tsao and B. D. Steinberg, *Reduction of sidelobe and speckle artifacts in microwave imaging*, IEEE Trans. Antennas Propag. **36** (1988), 543–556.
5. J. Li and P. Stoica, *Efficient mixed-spectrum estimation with applications to target feature extraction*, IEEE Trans. Signal Process. **44** (1996), no. 2, 281–295.
6. J. W. Odendaal, E. Barnard, and C. W. I. Pistorius, *Two-dimensional superresolution radar imaging using the MUSIC algorithm*, IEEE Trans. Antennas Propag. **42** (1994), no. 10, 1386–1391.
7. S. Rouquette and M. Najim, *Estimation of frequencies and damping factors by two-dimensional ESPRIT type methods*, IEEE Trans. Signal Process. **49** (2001), no. 1, 237–245.
8. J. Herd, S. Duffy, and D. Carlson, Low cost multifunction phased array radar concept, in Proc. IEEE Internat. Symp. Phased Array Syst. Technol. Conf. (Lexington, MA), Oct. 12–15, 2010, pp. 457–460.
9. B. Ozen and I. Erer, *Radar target recognition via 2-D sparse linear prediction in missing data case*, in Proc. Eur., Signal Process. Conf. (Budapest, Hungary), Aug. 29–Sept. 2, 2016, pp. 1–5.
10. D. L. Donoho, *Compressive sensing*, IEEE Trans. Inf. Theory **52** (2006), no. 4, 1289–1306.
11. L. C. Potter et al., *A GTD-based parametric model for radar scattering*, IEEE Trans. Antennas Propag. **43** (1995), no. 10, 1058–1067.

12. M. Elad, Sparse and Redundant Representation, Springer, New York, NY, 2010.

13. S. G. Mallat and Z. Zhang, *Matching pursuits with time-frequency dictionary*, IEEE Trans. Signal Process. **41** (1993), no. 12, 3397–3415.

14. J. A. Tropp, *Greed is good: Algorithms results for sparse approximation*, IEEE Trans. Inf. Theory **50** (2004), no. 10, 2231–2242.

15. J.-H. Bae et al., *Performance of sparse recovery algorithms for the reconstruction of radar images from incomplete RCS data*, IEEE Geosci. Remote Sens. Lett. **12** (2015), no. 4, 1–5.

16. Y. Wu et al., *Fast marginalized sparse Bayesian learning for 3-D interferometric ISAR image formation via super-resolution ISAR imaging*, IEEE J. Sel. Topics Appl. Earth Observ. Remote Sens. **8** (2016), no. 10, 4942–4951.

17. Z. Liu et al., *Dynamic ISAR imaging of maneuvering targets based on sequential SL0*, IEEE Geosci. Remote Sens. Lett. **10** (2013), no. 5, 1041–1045.

18. X. Hu et al., *Fast SL0 algorithm for 3D imaging using bistatic MIMO radar*, IET Signal Proc. **12** (2018), no. 8, 1017–1022.

19. S. Demirci and C. Ozdemir, *Compressed sensing-based imaging of millimeter-wave ISAR data*, Microw. Opt. Technol. Lett. **55** (2013), no. 12, 2967–2972.

20. A. M. Raeb and S. K. Syed-Yusof, *Performance analysis of compressed sensing given insufficient random measurements*, ETRI J. **35** (2013), no. 2, 200–206.

21. W. Rao et al., *Parametric sparse representation method for ISAR imaging of rotating targets*, IEEE Trans. Aerosp. Electron. Syst. **50** (2014), no. 2, 910–919.

22. S. Zhang et al., *High-resolution bistatic ISAR imaging based on two-dimensional compressed sensing*, IEEE Trans. Antennas Propag. **63** (2015), no. 5, 2098–2111.

23. G. Li et al., *Multi-target simultaneous ISAR imaging based on compressed sensing*, EURASIP J. Adv. Signal Process. **2016** (2016), no. 24, 1–11.

24. M.-S. Kang and K.-T. Kim, Compressive sensing approach for high-resolution ISAR image reconstruction and autofocus, in Proc. IET Internat. Radar Conf. (Nanjing, China), Oct. 17–19, 2018, pp. 1–6.

25. S.-T. Yang and H. Ling, *Application of compressive sensing to two-dimensional radar imaging using a frequency-scanned microstrip leaky wave antenna*, J. Electromagn. Eng. Sci. **17** (2017), no. 3, 113–119.

26. J.-H. Bae et al., *Compressive sensing-based algorithm for one-dimensional scattering center extraction*, Microw. Opt. Technol. Lett. **58** (2016), 1408–1415.

27. C. Ozdemir, Inverse synthetic aperture radar imaging with MATLAB algorithms, John Wiley & Sons, Hoboken, NJ, 2012.

28. A. Ghaffari, M. Babaie-Zadeh, and C. Jutten, Sparse decomposition of two dimensional signals, in Proc. IEEE Int. Conf. Acoust., Speech Signal Process. (Taipei, Taiwan), Apr. 2009, pp. 3157–3160.

29. I. F. Gorodnitsky and B. D. Rao, *Sparse signal reconstruction from limited data using FOCUSS: A re-weighted norm minimization algorithm*, IEEE Trans. Signal Process. **45** (1997), no. 3, 600–616.

30. K.-T. Kim et al., *NCTR research using POSTECH compact range*, in Proc. Antenna Meas. Techn. Assoc. (Denver, CO, USA), 2001, pp. 60–65.

AUTHOR BIOGRAPHIES

Ji-Hoon Bae received the BS degree in electronic engineering from Kyungpook National University, Daegu, Rep. of Korea, in 2000, and the MS and PhD degrees in electrical engineering from the Pohang University of Science and Technology, Pohang, Gyeongbuk, Rep. of Korea, in 2002 and 2016, respectively. From 2002 to 2019, he was a Principal Researcher with the Electronics and Telecommunications Research Institute, Daejeon, Rep. of Korea. He joined the faculty of the Department of AI and Big Data Engineering, Daegu Catholic University, Gyeongsan, Gyeongbuk, Rep. of Korea, in 2019. His research interests include deep learning, transfer learning, radar imaging, radar signal processing, and optimized techniques. He is a member of the Institute of Electrical and Electronics Engineers, Korea Institute of Electromagnetic Engineering and Science, and Institute of Electronics and Information Engineers.

Kyung-Tae Kim received the BS, MS, and PhD degrees in electrical engineering from Pohang University of Science and Technology (POSTECH), Pohang, Rep. of Korea, in 1994, 1996, and 1999, respectively. From 2002 to 2010, he was a Faculty Member with the Department of Electronic Engineering, Yeungnam University, Gyeongsan, Rep. of Korea. Since 2011, he has been with the Department of Electrical Engineering, POSTECH, where he is currently a Professor. From 2012 to 2017, he was the Director of the Sensor Target Recognition Laboratory, sponsored by the Defense Acquisition Program Administration and the Agency for Defense Development. He is the Director of the Unmanned Surveillance and Reconnaissance Technology Research Center and the Radar and ElectroMagnetics Signal Processing Laboratory, POSTECH. Since 2019, he has been the Director of the Center for Next Generation Imaging Radar System, sponsored by the Ministry of Science and ICT. He has authored approximately 200 papers in journals and conference proceedings. He is currently performing several research projects funded by the Government of South Korea and several industries. His research interests mainly include the domain of radar signal processing and system modeling: SAR/ISAR imaging, target recognition, direction-of-arrival estimation, micro-Doppler analysis, automotive radars, digital beamforming, electronic warfare, and electromagnetic scattering. He is a member of the Korea Institute of Electromagnetic Engineering and Science. He was a recipient of several outstanding research awards and best paper awards from KIEES and international conferences.